Analytical model of hydrogen inventory saturation in the subsurface of the wall material and comparison to Reaction-Diffusion simulations

J. Denis, E.A. Hodille, Y. Marandet, Y. Ferro

To cite this version:

J. Denis, E.A. Hodille, Y. Marandet, Y. Ferro. Analytical model of hydrogen inventory saturation in the subsurface of the wall material and comparison to Reaction-Diffusion simulations. Journal of Nuclear Materials, In press, 10.1016/j.jnucmat.2022.153972 . hal-03752707

HAL Id: hal-03752707
https://hal.science/hal-03752707v1

Submitted on 17 Aug 2022

Analytical model of hydrogen inventory saturation in the subsurface of the wall material and comparison to Reaction-Diffusion simulations.

J. Denis[a], E. A. Hodille[b], Y. Marandet[a], and Y. Ferro[a]

[a] *Aix-Marseille Univ., CNRS, PIIM, F-13013 Marseille, France.*
[b] *CEA, IRFM, F-13108 Saint-Paul-lez-Durance, France.*

e-mail address: julien.denis@univ-amu.fr

Abstract

We herein introduce an analytical model of hydrogen inventory saturation in the subsurface of materials (several micrometers depth) under plasma implantation. This model is valid for materials for which the desorption process is not limited by hydrogen recombination at the surface. It is based on a simplified assumption for the implantation of both hydrogen ions and atoms (point sources) and on a stationary approach. The model provides an approximation of the density profile of mobile/interstitial hydrogen and of the density profile of hydrogen trapped at materials defects in the subsurface layer. The analytical model shows good agreement with Reaction-Diffusion simulations of deuterium implantation in tungsten at different material temperatures. For the fusion relevant materials tungsten and beryllium, it is shown that most of the inventory is found in traps. The model gives the filling ratio of traps in the subsurface at steady-state $f_{\text{stat},i}^{\text{BULK}}$. This simple parameter indicates how the total subsurface inventory builds up during plasma exposure and provides a simple way to understand the retention dynamics observed during non-linear Reaction-Diffusion simulations.

1 Introduction.

The interaction of Hydrogen Isotopes (HI) with materials has attracted lots of attention in the past years, especially in the field of nuclear fusion. Future reactors will produce energy via nuclear fusion of deuterium and tritium nuclei. Part of the tritium will be retained in the wall of the reactor leading to safety issues as tritium is radioactive [1]. The two main mechanisms leading to HI retention are: (i) HI co-deposition with eroded wall materials [1] and (ii) HI implantation within the materials. The latter can be theoretically studied via the so-called Reaction-Diffusion (R-D) system of equations introduced by McNabb and Foster [2]. This system describes the implantation of HIs, their diffusion and trapping at defects into the materials. Since then, the R-D model has been numerically solved to study the interaction of HI with various fusion relevant materials: tungsten [3, 4, 5, 6, 7, 8], beryllium [9, 10], steel [11, 12], aluminium [13] to mention just a few examples.
However, in a tokamak, the implantation conditions vary widely as a function of the location on the wall; this complicates the full modelling of HI retention and the interpretation of the simulation results. Nonetheless, the first simulation of the dynamics of HI retention was recently performed at the scale of the JET tokamak [14]. But the R-D equations are non-linear, making the full understanding of the phenomenon they describe difficult. To achieve such an understanding, we here propose a simple analytical model.

In 1982, B. L. Doyle already introduced an analytical model based on a simplified description of the implantation source considered as a point [15]. Doyle also assumed that a steady state was reached. The mechanisms incorporated in the model were diffusion and surface recombination of HI, while trapping of HI at defects was omitted. As a consequence, the model provides only the interstitial/mobile HI density profiles, not the HIs density trapped at defects. Moreover, recent results have shown that the recombination model used by Doyle is dependent on the implantation flux density [16], and this dependence has not yet been theoretically established. More recent attempts were carried out to derive a time-dependent analytical model [17, 18]. This model has the advantage to consider trapped HIs and to follow their evolution in time. However, it is based on the assumption of deep trapping, which implies a high density of traps and that trapped HI cannot be released. Such an assumption implies low temperature and low implantation flux density, which limits the range of validity of the model. This range of validity has still not been evaluated yet.

It follows that the retention dynamics of HIs into the wall of tokamak would have its understanding facilitated by the availability of an analytical model considering implantation, diffusion, trapping and release, all of this in a broad range of temperature. This is precisely the aim of this work. The present model is based on the same assumptions as used by Doyle: (i) the implantation source is assumed as a point source, and (ii) the steady-state is reached. Trapping at various point defects is also considered while the recombination process is assumed not rate-limiting.

The rest of the paper is organised as follows. First the considered R-D system of equations is introduced. Then it is shown that the HI inventory calculated by this system tends to saturate during plasma exposure in a time scale similar to the one experimentally observed. An analytical model for hydrogen inventory saturation in the subsurface under plasma exposure is subsequently introduced and is compared to R-D simulations at different material temperatures. This model gives the expression of the filling ratio of traps in the subsurface at steady-state, $f_{\mathrm{stat},i}^{\mathrm{BULK}}$. We eventually determine which kind of implanted HIs (mobile or trapped) dominates the total subsurface inventory in fusion relevant material tungsten and beryllium. The article concludes by highlighting that the simple parameter $f_{\mathrm{stat},i}^{\mathrm{BULK}}$ is key to understand the dynamics of the total HI inventory in the subsurface of materials.

2 Reaction-Diffusion equations.

The analytical model is derived from the R-D system of equations [2]. According to McNabb and Foster, two HI populations are considered: mobile HI, which diffuses in the material by jumping from interstitial site to interstitial site, and trapped HI which are retained at lattice defects (also called traps). It is considered that these defects are saturable and can only accommodate a single HI. The model expresses the time evolution of the density of mobile HI, n_{m} [m^{-3}], and of the density of trapped HI at the trap of kind i, $n_{\mathrm{t},i}$ [m^{-3}]. The R-D system is made of a diffusion equation for the mobile particles (equation 1a) coupled to trapping-detrapping equations in various traps of kind i according to the reaction $\mathrm{HI_m} + \mathrm{Trap}_i \leftrightarrows \mathrm{HI}_{\mathrm{t},i}$ (equation 1b):

$$\left\{\begin{array}{ll}
\dfrac{\partial n_{\mathrm{m}}(x,t)}{\partial t} = \dfrac{\partial}{\partial x}\left(D(T)\dfrac{\partial n_{\mathrm{m}}}{\partial x}\right) - \displaystyle\sum_{i=1}^{N_{\mathrm{trap}}} \dfrac{\partial n_{\mathrm{t},i}}{\partial t} & \\
\qquad + S_{\mathrm{ext}}^{\mathrm{i+}}(x,t) + S_{\mathrm{ext}}^{\mathrm{at}}(x,t) & \text{(1a)} \\
\dfrac{\partial n_{\mathrm{t},i}(x,t)}{\partial t} = \nu_{\mathrm{t},i}^{*}(T)\dfrac{n_i(x) - n_{\mathrm{t},i}}{n_{\mathrm{IS}}} n_{\mathrm{m}} - \nu_{\mathrm{dt},i}(T) n_{\mathrm{t},i} & \text{(1b)} \\
\text{B.C. at } x = 0\text{: } n_{\mathrm{m}}(0,t) = 0 & \text{(1c)} \\
\text{B.C. at } x = L\text{: } \left|\begin{array}{l} n_{\mathrm{m}}(L,t) = 0 \\ \quad\text{or} \\ D(T)\dfrac{\partial n_{\mathrm{m}}}{\partial x}(L,t) = 0 \end{array}\right. & \text{(1d)}
\end{array}\right.$$

All the parameters and variables of this system of equations are given in table 1.

Variable or parameter	Definition	Units
x	Material depth	m
T	Material temperature	K
$D(T) = D_0 \exp\left(-E_{\text{diff}}/(k_{\text{B}}T)\right)$	Diffusion coefficient of HI in the material	$\text{m}^2.\text{s}^{-1}$
E_{diff}	Activation energy of diffusion	eV
k_{B}	Boltzmann constant	$\text{eV}.\text{K}^{-1}$
N_{trap}	Number of traps in the material	
$\nu^*_{\text{t},i}(T) = \nu^0_{\text{t},i} \exp\left(-E_{\text{t},i}/(k_{\text{B}}T)\right)$	Trapping attempt frequency in the trap of kind i	s^{-1}
$E_{\text{t},i}$	Activation energy of trapping	eV
$n_i(x)$	Trap density	m^{-3}
n_{IS}	Density of interstitial sites for HI	m^{-3}
$\nu_{\text{dt},i} = \nu^0_{\text{dt},i} \exp\left(-E_{\text{dt},i}/(k_{\text{B}}T)\right)$	Detrapping frequency	s^{-1}
$E_{\text{dt},i}$	Activation energy of detrapping	eV

Table 1: Variables and parameters of the Reaction-Diffusion equations.

The R-D equations consider the interaction between HI and material defects/traps. These traps can be intrinsic (i.e. due to the manufacturing process) like grain boundaries and impurities, or extrinsic, i.e. due to the plasma or neutron irradiation, like vacancies or bubbles. The latter traps depend on the material and on the experimental conditions. The number of traps N_{trap} is obtained by fitting of thermal-desorption analysis with the R-D equations 1, see for example references [5, 6, 7]. The fitting gives also the density profile of traps $n_i(x)$ and their detrapping energy $E_{\text{dt},i}$. It is possible to compare these detrapping energies to detrapping energies calculated with first-principle Density Functional Theory calculation for point defects (vacancy, di-vacancy, impurities) to characterise the type of defects present in the real material.

In equation 1a, implantation of ions and atoms from the plasma are given by two volume source, $S^{\text{i+}}_{\text{ext}}$ and $S^{\text{at}}_{\text{ext}}$ respectively:

$$S^j_{\text{ext}}(x,t) = \Gamma^j_{\text{imp}}(t) f^j_{\text{imp}}(x,t) \tag{2}$$

where $\Gamma^j_{\text{imp}}(t)$ is the particle implantation flux density and f^j_{imp} is the implantation profile. It is usually considered as a gaussian defined by a mean implantation range of particles $X^j_{\text{imp}}(t)$ [m] and a standard deviation $\sigma^j_{\text{imp}}(t)$. Both parameters depend on the HI impact energy, E^j_{imp} [eV], and on the angle of incidence with respect to the surface, α^j_{imp} [°]. They can be given by Binary Collision Approximation codes such as SRIM [19] or SDTrim.sp [20].

The system of equations 1 is solved using Boundary Conditions (B.C.) at both front ($x = 0$) and rear ($x = L$) surfaces. The choice of these B.Cs depends on the material. We here consider that HI recombination and desorption are immediate at the front surface of the material, yielding to the Dirichlet B.C equation 1c. On the rear side, either Dirichlet or Neumann B.C., equations 1d, is assumed depending on the material.

3 Hydrogen inventory saturation in the subsurface under plasma implantation.

In fusion devices, it is experimentally observed through gas balance analysis that saturation of HI retention due to implantation in the wall is achieved within 1 to 100 s. This characteristic time depends on the wall materials and on the plasma scenario [21, 22, 23]. By nature, such a saturation process has to be reproduced by the non-linear R-D model presented above. The code Migration of Hydrogen Isotopes in MaterialS (MHIMS) [7, 18] features an implementation of the R-D equations

1. The saturation process is further investigated with MHIMS via the modelling of deuterium (D) implantation in a tungsten (W) wall at three different implantation temperatures: 300 K, 500 K and 800 K. A 1 mm depth W sample is loaded with both D^+ and D. The implantation conditions (flux density and energy, the same for the three simulations - shown in table 2) are chosen consistent with divertor conditions. The parameterisation of the R-D equations defined by Hodille et al. for D-W interaction [18] is also used and is given in Appendix A. The W sample presents 3 traps for D with respective profiles and detrapping energies reported in figure 7 in Appendix A.

Implantation parameters	D^+	D
$\mathit{\Gamma}^j_{\mathrm{imp}}$ [$\mathrm{m^{-2}.s^{-1}}$]	1.0×10^{21}	0.5×10^{21}
E^j_{imp} [eV]	100	50
α^j_{imp} [°]	90	90
X^j_{imp} [nm]	2.7	1.8

Table 2: Implantation parameters for both D^+ and D considered in the simulation of D implantation in W. They correspond to divertor-like conditions. The angle of incidence α^j_{imp} is given with respect to the material surface. The values of the corresponding mean implantation ranges $X^{\mathrm{i+}}_{\mathrm{imp}}$ and $X^{\mathrm{at}}_{\mathrm{imp}}$ calculated by the SRIM code are also given.

The MHIMS code provides the D desorption flux density $\mathit{\Gamma}_{\mathrm{out}}$ [$\mathrm{m^{-2}.s^{-1}}$], defined as the diffusive flux density at the material surface. $\mathit{\Gamma}_{\mathrm{out}}$ is expressed in terms of D atoms (not D_2 molecules) to be compared to the implantation flux densities of D ions and atoms. This comparison is achieved through a phenomenological coefficient often referred to as *molecular recycling coefficient*, R_{m}:

$$R_{\mathrm{m}}(t) = \frac{\mathit{\Gamma}_{\mathrm{out}}(t)}{\mathit{\Gamma}^{\mathrm{i+}}_{\mathrm{imp}}(t) + \mathit{\Gamma}^{\mathrm{at}}_{\mathrm{imp}}(t)} \tag{3}$$

In figure 1.a, the time evolution of the molecular recycling coefficient is displayed for the three different implantation temperatures: R_{m} tends to 1 in all the three cases within 1 to 100 s depending on the temperature as observed experimentally. The derivative of the total D areal inventory, Inv [$\mathrm{HI.m^{-2}}$], tends simultaneously to zero.

The relation between R_{m} and $dInv/dt$ is analysed below. To this end, the diffusion equation 1a is reformulated as follows:

$$\frac{\partial}{\partial t}\left(n_{\mathrm{m}}(x,t) + \sum_{i=1}^{N_{\mathrm{trap}}} n_{\mathrm{t},i}(x,t)\right) = \frac{\partial}{\partial x}\left(D(T)\frac{\partial n_{\mathrm{m}}}{\partial x}\right) + S^{\mathrm{i+}}_{\mathrm{ext}}(x,t) + S^{\mathrm{at}}_{\mathrm{ext}}(x,t) \tag{4}$$

The sum in parenthesis in the left-hand side is the total HI density. The total HI areal inventory is obtained through spatial integration of this equation:

$$\begin{aligned}\int_0^L \frac{\partial}{\partial t}\left(n_{\mathrm{m}}(x,t) + \sum_{i=1}^{N_{\mathrm{trap}}} n_{\mathrm{t},i}(x,t)\right) dx &= \int_0^L \frac{\partial}{\partial x}\left(D(T)\frac{\partial n_{\mathrm{m}}}{\partial x}\right) dx + \int_0^L S^{\mathrm{i+}}_{\mathrm{ext}}(x,t)dx + \int_0^L S^{\mathrm{at}}_{\mathrm{ext}}(x,t)dx \\ \frac{dInv(t)}{dt} &= \cancel{D(T)\frac{\partial n_{\mathrm{m}}}{\partial x}(L,t)} - D(T)\frac{\partial n_{\mathrm{m}}}{\partial x}(0,t) + \mathit{\Gamma}^{\mathrm{i+}}_{\mathrm{imp}}(t) + \mathit{\Gamma}^{\mathrm{at}}_{\mathrm{imp}}(t)\end{aligned} \tag{5}$$

From the MHIMS simulation at high temperature (800 K), one can see that the desorption flux density at the rear surface at $x = L$ (the first term in the right-hand side of the last equation of equations 5) is negligible even after 1000 s (the mobile D did not reach the rear boundary of the material). In addition, one can recognise the outgassing flux density $\mathit{\Gamma}_{\mathrm{out}}$ in the second term of the right-hand side

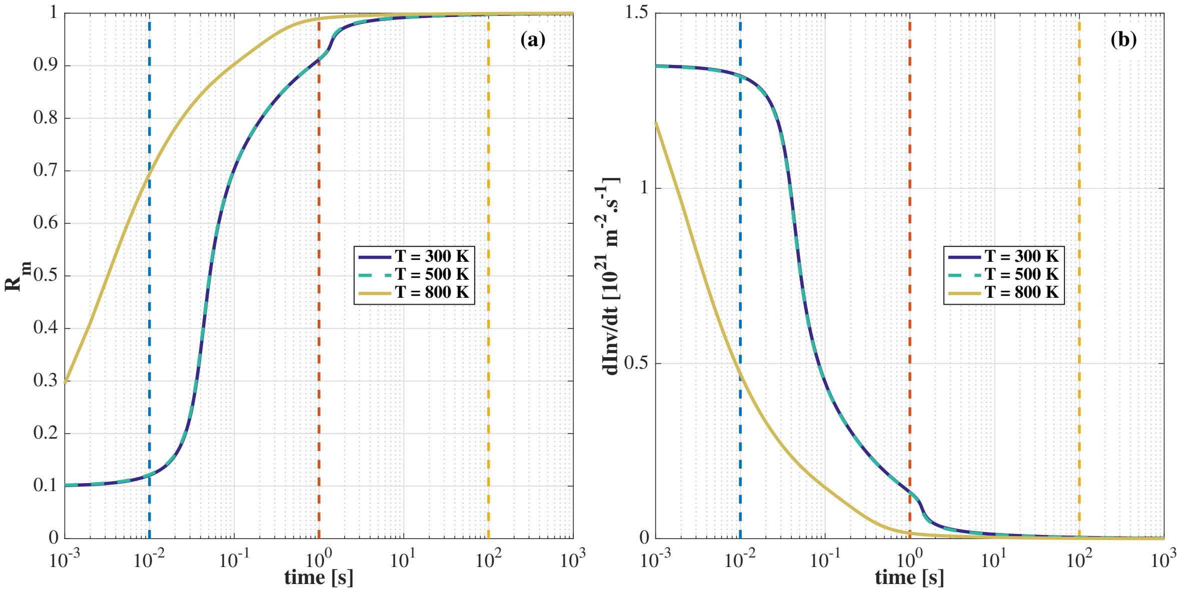

Figure 1: Time evolution of the molecular recycling coefficient R_{m} (a) and of the time derivative of the total D areal inventory (b) for a simulation of implantation of D in a W sample. The implantation parameters are listed in table 2 while the parameters for D–W interaction considered in MHIMS are summed up in Appendix A. The implantation is performed at three different sample temperatures: 300 K, 500 K and 800 K. The plots for $T = 300$ K and $T = 500$ K overlap. For all the simulations, R_{m} tends to 1 indicating a saturation of the wall inventory. The vertical dashed lines indicate the three times at which the density profiles of mobile and trapped particles are plotted in figures 3, 4 and 5.

of the same equation. Therefore equation 5 can be reformulated to express the relation between R_{m} and Inv:

$$\begin{aligned} R_{\mathrm{m}}(t) &= \frac{\Gamma_{\mathrm{out}}(t)}{\Gamma^{\mathbf{i}+}_{\mathrm{imp}}(t) + \Gamma^{\mathrm{at}}_{\mathrm{imp}}(t)} \\ R_{\mathrm{m}}(t) &= 1 - \frac{dInv(t)}{dt} \times \frac{1}{\Gamma^{\mathbf{i}+}_{\mathrm{imp}}(t) + \Gamma^{\mathrm{at}}_{\mathrm{imp}}(t)} \end{aligned} \tag{6}$$

From equation 6, one can easily see that R_{m} tends to 1 when the following condition is verified:

$$R_{\mathrm{m}}(t) \to 1 \Leftrightarrow \frac{dInv(t)}{dt} \ll \Gamma^{\mathbf{i}+}_{\mathrm{imp}}(t) + \Gamma^{\mathrm{at}}_{\mathrm{imp}}(t) \tag{7}$$

This condition indicates that R_{m} tends to unity when the evolution of the inventory is low w.r.t. the total implantation flux density. Such a condition is especially true when the subsurface inventory saturates. As a consequence, $dInv(t)/dt$ tends to 0 simultaneously as R_{m} tends to 1. This indicates saturation of the subsurface region and is consistent with results displayed in figure 1.a and 1.b. This is also consistent with experimental observations of saturation of the wall inventory. In the following, a simplified analytical model is derived to understand qualitatively this saturation process.

4 Analytical model for hydrogen inventory saturation in the subsurface under plasma implantation.

The analytical model is based on the same simplified description of material implantation as used by B. L. Doyle [15]. The external source S^*_{ext} is considered as point source at a depth X^*_{imp} equal to the mean implantation depth. In this work, we consider two sources of implantation: a ionic one, $S_{\text{ext}}^{\text{i+}}$, and an atomic one, $S_{\text{ext}}^{\text{at}}$. Which source implants deeper has no importance; we will only consider source 1 S_1 and source 2 S_2 such as $X_{\text{imp},1} < X_{\text{imp},2}$ (with $S_1 = S_{\text{ext}}^{\text{i+}}$ or $S_{\text{ext}}^{\text{at}}$ and reversely for S_2). The temperature in the material is assumed constant in space and time. Moreover, we consider that the HI inventory has saturated and consequently that a steady-state has been reached. Under all these assumptions, the diffusion equation in the R-D model becomes:

$$\frac{\partial}{\partial x}\left(D(T)\frac{\partial n_{\text{m}}}{\partial x}\right) + \mathit{\Gamma}_{\text{imp},1}\delta(x - X_{\text{imp},1}) + \mathit{\Gamma}_{\text{imp},2}\delta(x - X_{\text{imp},2}) = 0 \tag{8}$$

Equation 8 can be solved assuming the Dirichlet B.C. at the front surface, equation 1c, and either the Dirichlet B.C. or the Neumann B.C at the rear surface, equations 1d. For both cases of B.C. at the rear surface, the overall density profiles of mobile particle displayed in figure 2 is linear by parts and only differs for $x > X_{\text{imp},2}$ depending on the B.C. used.

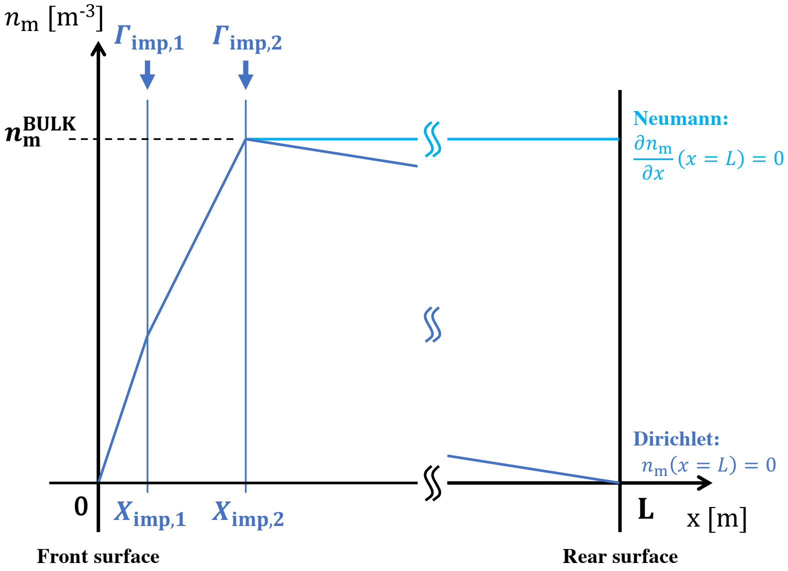

Figure 2: Schematic of the steady-state density profile of mobile HI in the simplified description of HI implantation in material. The two externals sources of implantation are considered as point sources at their respective mean implantation ranges $x = X_{\text{imp},1}$ and $x = X_{\text{imp},2}$. The two different bulk profiles (for $X_{\text{imp},2} \leq x \leq L$), corresponding to the use of a Dirichlet boundary condition (dark blue line) and of a Neumann boundary condition (light blue line) at the rear surface are also depicted.

Under realistic implantation conditions in fusion devices, the HI mean ranges $X_{\text{imp},1}$ and $X_{\text{imp},2}$ do not exceed 50 nm. Dirichlet B.C. at the rear surface is often used for massive surface material with a thickness L of several millimeters. However, since $X_{\text{imp},i} \ll L$, the gradient of n_{m} in the zone $[X_{\text{imp},2}, L]$ is weak, and when focusing on the front surface up to a length referred to as $k_{\%}L$, both Dirichlet and Neumann B.C. lead to the same solutions given below in equation 9:

$$\begin{cases}
\forall\ x \in [0, X_{\text{imp},1}],\ n_{\text{m}}(x) = \left[\frac{\mathit{\Gamma}_{\text{imp},1}}{D(T)} + \frac{\mathit{\Gamma}_{\text{imp},2}}{D(T)}\right] x & \text{(9a)} \\
\forall\ x \in [X_{\text{imp},1}, X_{\text{imp},2}],\ n_{\text{m}}(x) = \frac{\mathit{\Gamma}_{\text{imp},2}}{D(T)} x + \frac{\mathit{\Gamma}_{\text{imp},1}}{D(T)} X_{\text{imp},1} & \text{(9b)} \\
\forall\ x \in [X_{\text{imp},2}, k_{\%}L],\ n_{\text{m}}(x) = \frac{\mathit{\Gamma}_{\text{imp},2}}{D(T)} X_{\text{imp},2} + \frac{\mathit{\Gamma}_{\text{imp},1}}{D(T)} X_{\text{imp},1} = \boldsymbol{n}_{\mathbf{m}}^{\mathbf{BULK}} & \text{(9c)}
\end{cases}$$

where equation 9c defines the maximum value of the density $n_{\mathrm{m}}^{\mathrm{BULK}}$ extending in the bulk direction. For the case a Neumann B.C. at $x = L$, this profile is the exact solution of the diffusion equation 8 and is valid for the whole material length ($k_{\%} = 100$ %). Regarding the case of a Dirichlet B.C. at $x = L$, this profile is an approximation of the exact profile. If one considers an absolute error of $k_{\%} n_{\mathrm{m}}^{\mathrm{BULK}}$ on n_{m} (hence a maximum relative error $k_{\%}$ for $x > X_{\mathrm{imp},2}$), this approximation is valid for $L \gg X_{\mathrm{imp},2}/k_{\%}$ up to a depth $x = k_{\%} L$ (cf. Appendix B). For example, in the MHIMS simulations presented in section 3, $L = 1$ mm and $X_{\mathrm{imp},2} = 2.7$ nm: assuming a relative error $k_{\%} = 1$ %, the approximated profile given by equation 9 is valid up to $x = 10$ μm.
Then one can obtain the outgassing flux density from equation 9a:

$$\mathit{\Gamma}_{\mathrm{out}} = D(T)\frac{\partial n_{\mathrm{m}}}{\partial x}(0) = \mathit{\Gamma}_{\mathrm{imp},1} + \mathit{\Gamma}_{\mathrm{imp},2} \tag{10}$$

And the resulting molecular recycling coefficient is:

$$R_{\mathrm{m}} = \frac{\mathit{\Gamma}_{\mathrm{out}}}{\mathit{\Gamma}_{\mathrm{imp},1} + \mathit{\Gamma}_{\mathrm{imp},2}} = 1 \tag{11}$$

which verifies the condition of full recycling.

Now, we focus on the profile of trapped particles. At steady-state, equation 1b gives:

$$\frac{\partial n_{\mathrm{t},i}(x,t)}{\partial t} = 0 \Leftrightarrow n_{\mathrm{t},i}(x) = \frac{n_i(x)}{1 + \dfrac{\nu_{\mathrm{dt},i}(T)}{\nu^*_{\mathrm{t},i}(T)}\dfrac{n_{\mathrm{IS}}}{n_{\mathrm{m}}(x)}} \tag{12}$$

We obtain the density profiles of trapped HI at steady-state by inserting $n_{\mathrm{m}}(x)$ from equation 9 in equation 12. We then define the stationary filling ratio for each trap of kind i by:

$$f_{\mathrm{stat},i}(x) = \frac{n_{\mathrm{t},i}(x)}{n_i(x)} = \frac{1}{1 + \dfrac{\nu_{\mathrm{dt},i}(T)}{\nu^*_{\mathrm{t},i}(T)}\dfrac{n_{\mathrm{IS}}}{n_{\mathrm{m}}(x)}} \tag{13}$$

Inserting the maximum density of mobile $n_{\mathrm{m}}^{\mathrm{BULK}}$ (equation 9c) into equation 13 leads to the stationary bulk filling ratio for each trap of kind i:

$$\begin{aligned} f_{\mathrm{stat},i}^{\mathrm{BULK}} &= \frac{1}{1 + \dfrac{\nu_{\mathrm{dt},i}(T)}{\nu^*_{\mathrm{t},i}(T)}\dfrac{n_{\mathrm{IS}}}{n_{\mathrm{m}}^{\mathrm{BULK}}}} = \frac{1}{1 + \dfrac{\nu_{\mathrm{dt},i}(T)}{\nu^*_{\mathrm{t},i}(T)}\dfrac{n_{\mathrm{IS}}D(T)}{\mathit{\Gamma}_{\mathrm{imp},1}X_{\mathrm{imp},1} + \mathit{\Gamma}_{\mathrm{imp},2}X_{\mathrm{imp},2}}} \\ f_{\mathrm{stat},i}^{\mathrm{BULK}} &= \frac{1}{1 + \dfrac{\nu^0_{\mathrm{dt},i}}{\nu^0_{\mathrm{t},i}}\dfrac{n_{\mathrm{IS}}D_0}{\mathit{\Gamma}_{\mathrm{imp},1}X_{\mathrm{imp},1} + \mathit{\Gamma}_{\mathrm{imp},2}X_{\mathrm{imp},2}}\exp\left(\dfrac{-E_{\mathrm{b},i} - E_{\mathrm{diff}}}{k_{\mathrm{B}}T}\right)} \end{aligned} \tag{14}$$

where the binding energy of HI to the trapping site i is $E_{\mathrm{b},i} = E_{\mathrm{dt},i} - E_{\mathrm{t},i}$. The expression of $f_{\mathrm{stat},i}^{\mathrm{BULK}}$ is further simplified assuming that only diffusion limits trapping, which implies $\nu^*_{\mathrm{t},i}(T) = D(T)/\lambda^2$, as in section 3:

$$\begin{aligned} f_{\mathrm{stat},i}^{\mathrm{BULK}} &= \frac{1}{1 + \dfrac{\nu_{\mathrm{dt},i}(T)\lambda^2 n_{\mathrm{IS}}}{\mathit{\Gamma}_{\mathrm{imp},1}X_{\mathrm{imp},1} + \mathit{\Gamma}_{\mathrm{imp},2}X_{\mathrm{imp},2}}} \\ f_{\mathrm{stat},i}^{\mathrm{BULK}} &= \frac{1}{1 + \dfrac{\nu_{\mathrm{dt},i}(T)}{\nu_{\mathrm{t}}^{\mathrm{BULK}}(\mathit{\Gamma}_{\mathrm{imp},1}, X_{\mathrm{imp},1}, \mathit{\Gamma}_{\mathrm{imp},2}, X_{\mathrm{imp},2})}} \end{aligned} \tag{15}$$

This expression is of a central importance for the rest of this work. Since $f_{\mathrm{stat},i}^{\mathrm{BULK}} = n_{\mathrm{t},i}^{\mathrm{BULK}}(x)/n_i(x)$, it allows to determine if trap i is filled or empty. More precisely, in equation 15, $f_{\mathrm{stat},i}^{\mathrm{BULK}}$ presents a ratio between the detrapping frequency from trap i ($\nu_{\mathrm{dt},i}$), which only depends on the material temperature, and $\nu_{\mathrm{t}}^{\mathrm{BULK}}$ or maximum trapping frequency, which only depends on the implantation conditions (flux densities and mean implantation ranges). The comparison between $\nu_{\mathrm{dt},i}$ and $\nu_{\mathrm{t}}^{\mathrm{BULK}}$ enables to highlight the process that dominates the interaction between D and traps:

- when $\nu_{\mathrm{dt},i} \gg \nu_{\mathrm{t}}^{\mathrm{BULK}}$, detrapping is more efficient than trapping, $f_{\mathrm{stat},i}^{\mathrm{BULK}}$ tends to 0 and the trap i remains empty.
- when $\nu_{\mathrm{dt},i} = \nu_{\mathrm{t}}^{\mathrm{BULK}}$, $f_{\mathrm{stat},i}^{\mathrm{BULK}}$ is equal to 0.5 and the trap i is half filled with HI.
- when $\nu_{\mathrm{dt},i} \ll \nu_{\mathrm{t}}^{\mathrm{BULK}}$, trapping is more efficient than detrapping, $f_{\mathrm{stat},i}^{\mathrm{BULK}}$ tends to 1 and the trap i saturates.

5 Comparison of the analytical model with Reaction-Diffusion simulations.

The analytical model described in the previous section is now compared to the R-D simulations performed with the MHIMS code and presented in section 3. The aim is to estimate the validity of the analytical model in the full range of temperature found in the materials of fusion devices. The profiles simulated by MHIMS are extracted at three times during the simulations: 0.01 s, 1 s and 100 s (cf. figure 1). At $t = 0.01$ s, R_{m} is way below 1 for the three implantation temperatures, $T = 300$ K, 500 K and 800 K. At $t = 1$ s, R_{m} is around 0.9 for $T = 300$ K and 500 K, while it saturates at $R_{\mathrm{m}} = 1$ for $T = 800$ K. At $t = 100$ s, R_{m} saturates at 1 for the three simulations and full saturation of subsurface inventory is expected.

The density profiles of mobile particles n_{m} are plotted at $t = 0.01$ s, 1 s and 100 s for the three implantation temperatures of 300 K, 500 K and 800 K in figures 3.a, 3.b and 3.c respectively. The analytical density profiles obtained from equation 9 are also displayed as well as the mean implantation ranges for ions $X_{\mathrm{imp}}^{\mathrm{i+}}$ and for atoms $X_{\mathrm{imp}}^{\mathrm{at}}$ (whose values are reported in table 2). A very good agreement between the analytical profiles and the simulated profiles is observed in the implantation zone ($0 \leq x \leq 30$ nm) for the cases where $R_{\mathrm{m}} = 1$. This corresponds to $t = 100$ s for the three implantation temperatures and to $t = 1$ s for $T = 800$ K. On the contrary, at $t = 0.01$ s for the three temperatures, the density profile of mobile still builds up, and at $t = 1$ s for $T = 300$ K and 500 K, the diffusion front in the depth of the material is not distant enough from the implantation zone to have an almost flat density profile of mobile in the zone $x > X_{\mathrm{imp},2}$. It is clear that the density profiles for each implantation temperature tend to the analytical profiles when the implantation time increases. Thus, equation 9 can be seen as an upper limit to the density profile of mobile particles in the subsurface.

In the same way, the analytical density profiles of trapped particle $n_{\mathrm{t},i}$ given by equation 12 are compared to the one simulated by MHIMS. Figures 4 and 5 display $n_{\mathrm{t},i}$ for traps 1 and 3, respectively, during the same simulations as above. These traps are arbitrarily selected due to their highly different detrapping energies and density profiles. For the sake of clarity, the results for trap 2 are not shown; they are similar to the ones for traps 1 and 3. The same conclusions as for n_{m} can be drawn for $n_{\mathrm{t},i}$: (i) a very good agreement is found between the analytical and the simulated profiles in the implantation zone ($0 \leq x \leq 30$ nm) when $R_{\mathrm{m}} = 1$, and (ii) the profiles for each implantation temperature tend to the analytical profiles when the implantation time increases. The agreement is particularly good in case of trap 3, whose density profile is non-uniform. Thus, the analytical profile given by equation 12 can also be seen as an upper limit to the profile of $n_{\mathrm{t},i}$ to which the R-D model converges at the subsurface.

Finally, the bulk filling ratio at steady state $f_{\mathrm{stat},i}^{\mathrm{BULK}}$ is given in inset for the three simulations in figure 4 for trap 1 and in figure 5 for trap 3. At 300 K both traps are fully saturated. At 500 K, trap 3 is still saturated while trap 1 remains empty during implantation with a bulk filling ratio of 3 %. At 800 K, trap 1 is completely empty while trap 3 is partially filled with $f_{\mathrm{stat},3}^{\mathrm{BULK}} = 17$ %. Overall, trap 3 retains more efficiently D due to its higher detrapping energy.

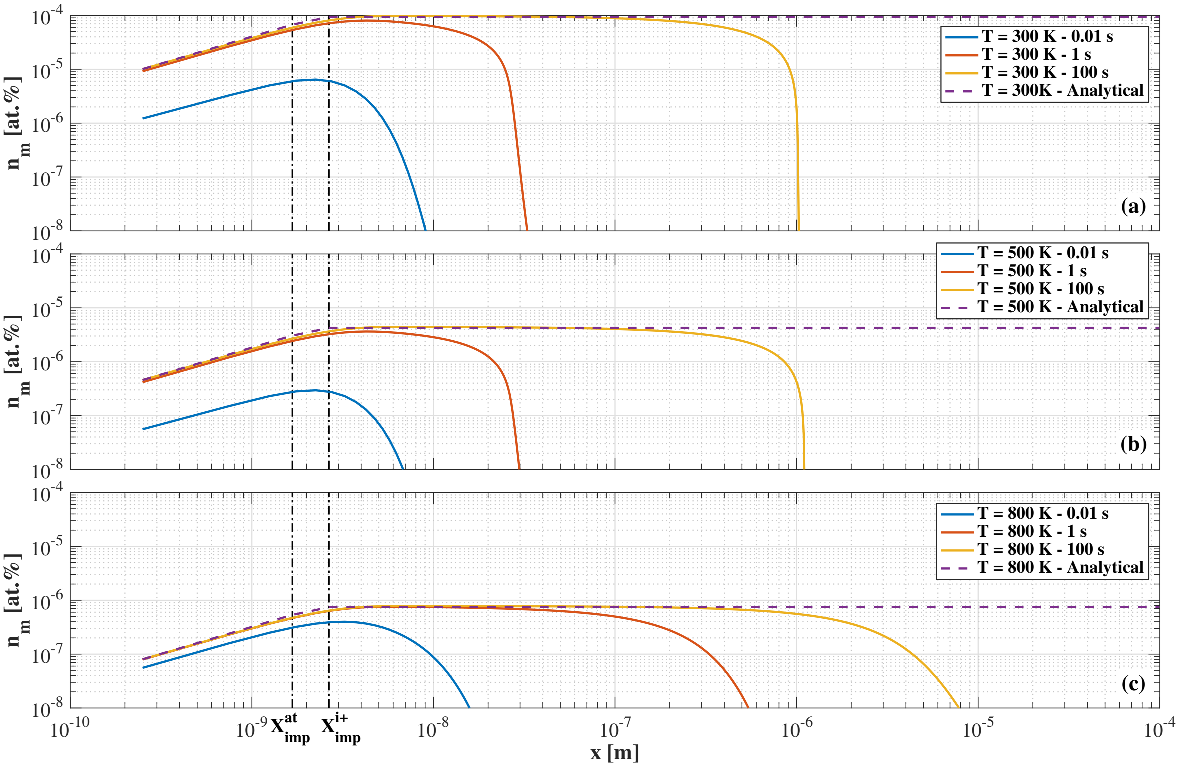

Figure 3: Density profile of mobile D obtained in the simulation of D implantation in a W sample with MHIMS. The profiles are plotted for three different times in the simulation: 0.01 s, 1 s and 100 s. The implantation is performed at three different sample temperatures: 300 K, 500 K and 800 K. The respective profiles are plotted in figures (a), (b) and (c). The analytical density profiles obtained from equation 9 are also plotted. The density is expressed in at.% of W. The implantation mean ranges for ions $X_{\mathrm{imp}}^{\mathrm{i+}}$ and for atoms $X_{\mathrm{imp}}^{\mathrm{at}}$ in the simulations are also indicated.

To conclude, the analytical model shows a very good agreement with Reaction-Diffusion equations in the subsurface layer of materials. It is however based on three assumptions whose relevance is discussed below in the context of fusion devices:

(i) Constant temperature in space and time: in fusion devices, most of the wall is submitted to very low heat fluxes and therefore stays at the initial wall temperature. Only the divertor region is submitted to strong heat fluxes and exhibits strong temperature excursions. However, with actively-cooled plasma-facing components, the wall temperature, including the divertor, reaches a steady-state after 5 to 10 s depending on the component design, making the approximation valid in time. It is also valid in space, with a temperature variation below 1 K in the first ten micrometers of both W and Be under divertor-like heat flux densities (10 $\mathrm{MW.m^{-2}}$).

(ii) Steady-state: as shown in figures 3, 4 and 5, steady-state is quickly reached in the subsurface layer, after ~ 1 s for the three considered temperatures, making the steady-state approximation valid. To estimate a lower bound for the time to reach steady-state, a similar simulation has been performed with a lower implantation flux density (1×10^{19} $\mathrm{m^{-2}.s^{-1}}$) and low temperature (300 K). In these conditions, saturation of the wall (initially empty) occurs after 230 s, which may seem too long to validate the assumption. However, at such temperature, HI are not released from traps after a discharge and this time represents a cumulative plasma time: the subsurface traps are saturated after some twenty plasma discharges after which the time to reach steady-state will

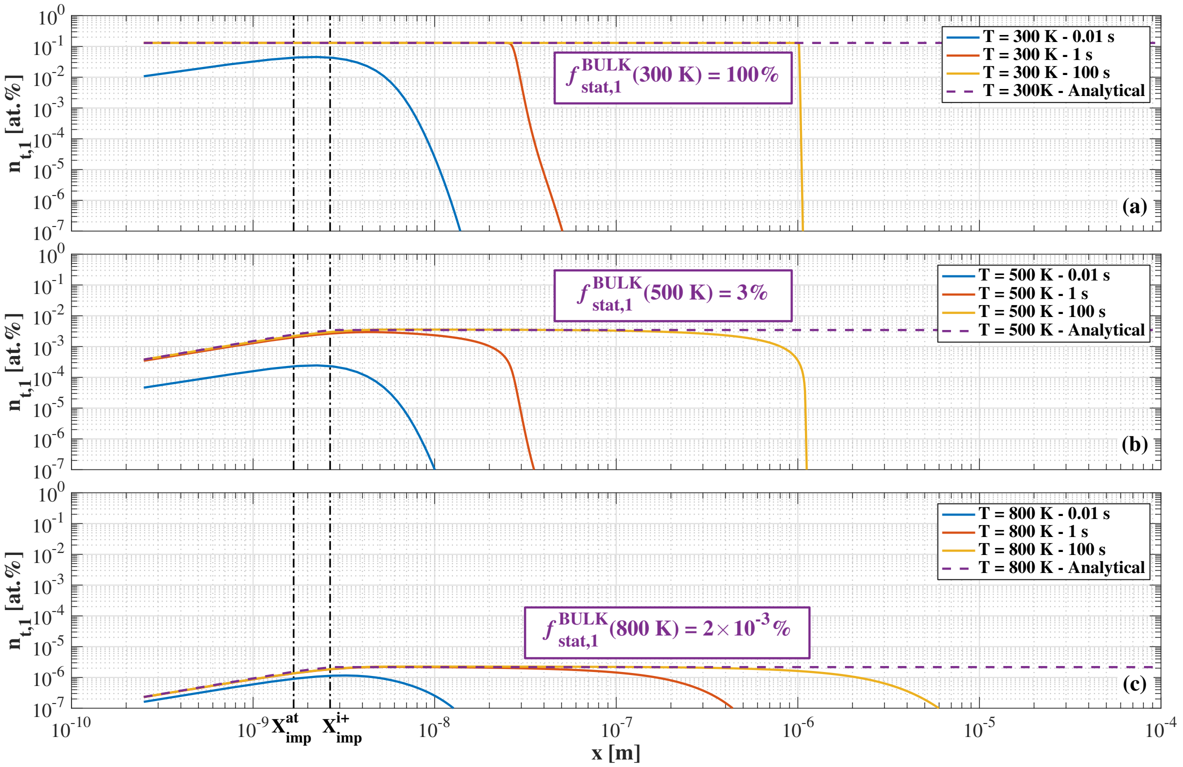

Figure 4: Density profile of D trapped in trap 1 obtained in the simulation of D implantation in a W sample with MHIMS. The profiles are plotted for three different times in the simulation: 0.01 s, 1 s and 100 s. The implantation is performed at three different sample temperatures: 300 K, 500 K and 800 K. The respective profiles are plotted in figures (a), (b) and (c). The analytical density profiles of trapped D, obtained from equation 12, are also plotted. Trap 1 presents a flat profile in all the material depth (cf. figure 7). The mean implantation ranges for ions $X^{\mathrm{i+}}_{\mathrm{imp}}$ and for atoms $X^{\mathrm{at}}_{\mathrm{imp}}$ in the simulations are also indicated. The bulk filling ratio of the trap at steady-state $f^{\mathrm{BULK}}_{\mathrm{stat,1}}$, as defined by equation 14, is also given for the three implantation temperatures.

be shorter and the approximation of a quick steady-state becomes valid.

(iii) Point sources for implantation: this point is discussed in appendix C, in which realistic gaussian sources have been considered and where the exact solutions of the diffusion equation 1a were derived at steady-state. It is shown that the point source assumption entails a maximum error on $n^{\mathrm{BULK}}_{\mathrm{m}}$ of 5 % for W and of 6 % to 12 % for Be depending on the HI angle of incidence. Concerning $f^{\mathrm{BULK}}_{\mathrm{stat},i}$, the relative error is below the errors reported for $n^{\mathrm{BULK}}_{\mathrm{m}}$.

6 A hydrogen isotopes subsurface inventory dominated by traps.

The analytical model here proposed provides good estimates of the density of mobiles n_{m} and the density of trapped HIs $n_{\mathrm{t},i}$ in the subsurface at steady-state. It allows to define a bulk filling ratio of traps at steady-state $f^{\mathrm{BULK}}_{\mathrm{stat},i}$. It follows that, given the knowledge of the density of traps i $n_i(x)$, $f^{\mathrm{BULK}}_{\mathrm{stat},i}$ determines an upper limit to which $n_{\mathrm{t},i}$ tends in time: $n^{\mathrm{BULK}}_{\mathrm{t},i}(x) = f^{\mathrm{BULK}}_{\mathrm{stat},i} n_i(x)$. As the implantation ranges $X_{\mathrm{imp},i}$ are in the order of few nanometers for both ions and atoms, the majority of the HI inventory is found in the bulk direction ($x > X_{\mathrm{imp},2}$). As a consequence, in case HIs would reside mostly in traps (as opposed to HIs as mobile), the knowledge of only $f^{\mathrm{BULK}}_{\mathrm{stat},i}$ would fully provide the

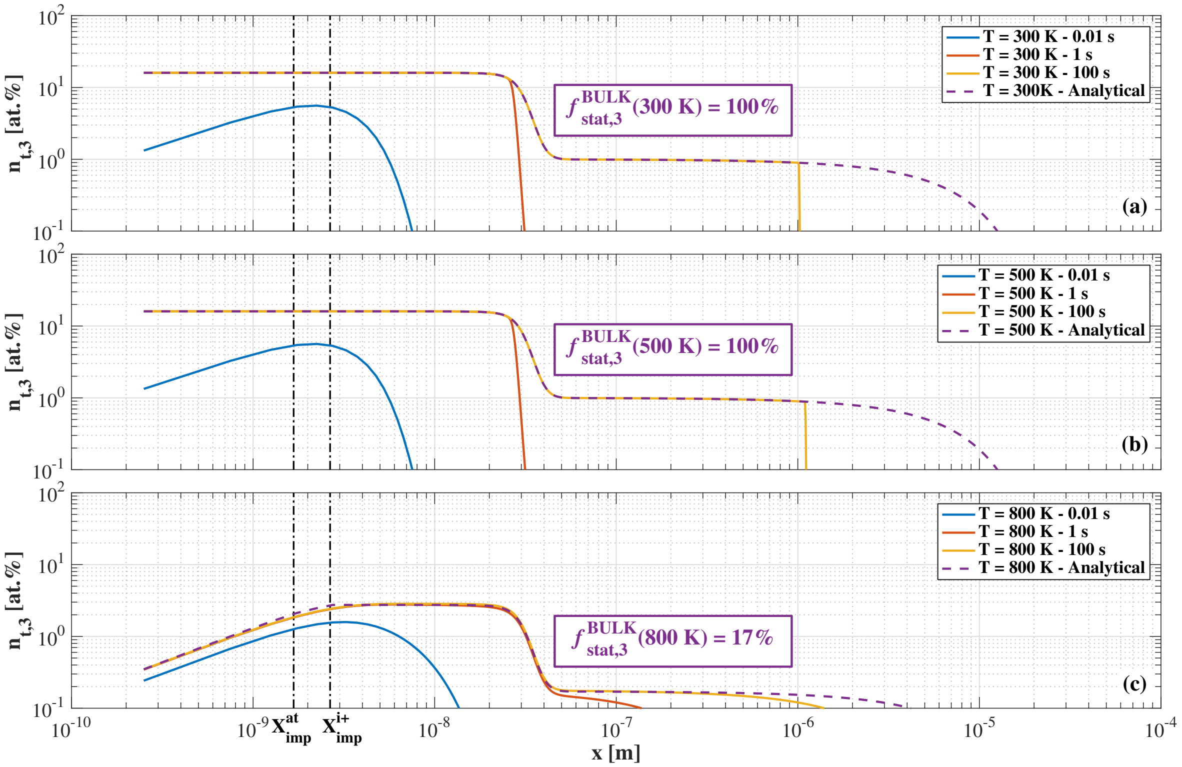

Figure 5: Density profile of D trapped in trap 3 obtained in the simulation of D implantation in a W sample with MHIMS. The profiles are plotted for three different times in the simulation: 0.01 s, 1 s and 100 s. The implantation is performed at three different sample temperatures: 300 K, 500 K and 800 K. The respective profiles are plotted in figures (a), (b) and (c). The analytical density profiles of trapped D, obtained from equation 12, are also plotted. Trap 3 is an ion-induced trap presenting two damaged zones (cf. figure 7) which explains the highly non-uniform profiles of trapped D observed in these figures. The mean implantation ranges for ions $X_{\text{imp}}^{\text{i+}}$ and for atoms $X_{\text{imp}}^{\text{at}}$ in the simulations are also indicated. The bulk filling ratio of the trap at steady-state $f_{\text{stat},3}^{\text{BULK}}$, as defined by equation 14, is also given for the three implantation temperatures.

limit to the total HIs inventory into the subsurface. Whether or not HIs reside in traps is analysed below.

Looking at figures 3, 4 and 5, we note that $n_{\text{t},i}$ is much higher than n_{m} for the three implantation temperatures in all the material depth. To verify if this is always true, we can look at the ratio between the maximum density of trapped HIs and the maximum density of mobile HIs:

$$\begin{aligned}
\frac{n_{\text{t},i}^{\text{BULK}}(x)}{n_{\text{m}}^{\text{BULK}}} \gg 1 &\Leftrightarrow \frac{f_{\text{stat},i}^{\text{BULK}} n_i(x)}{n_{\text{m}}^{\text{BULK}}} \gg 1 \\
\frac{n_{\text{t},i}^{\text{BULK}}(x)}{n_{\text{m}}^{\text{BULK}}} \gg 1 &\Leftrightarrow n_i(x) \gg \underbrace{n_{\text{m}}^{\text{BULK}} + \frac{\nu_{\text{dt},i}(T)}{\nu_{\text{t},i}^{*}(T)} n_{\text{IS}}}_{n_i^{\text{MIN}}}
\end{aligned} \qquad (16)$$

From equation 16, if the density of traps n_i is way above a threshold value called n_i^{MIN}, the subsurface inventory will mostly resides in traps at steady-state. n_i^{MIN} is a sum of two terms. The first one is $n_{\text{m}}^{\text{BULK}}$, equation 9c, and only depends on the implantation conditions and on the diffusion coefficient.

The second one depends on the ratio between the detrapping frequency and the trapping frequency (hence function of the trap binding energy), making n_i^{MIN} strongly dependent on the material temperature. The expression of n_i^{MIN} is further simplified assuming that only diffusion limits trapping, which implies $\nu_{\mathrm{t},i}^*(T) = D(T)/\lambda^2$:

$$n_i^{\mathrm{MIN}} = \frac{\Gamma_{\mathrm{imp},2} X_{\mathrm{imp},2} + \Gamma_{\mathrm{imp},1} X_{\mathrm{imp},1}}{D(T)} + \frac{\nu_{\mathrm{dt},i}(T)\lambda^2}{D(T)} n_{\mathrm{IS}} \tag{17}$$

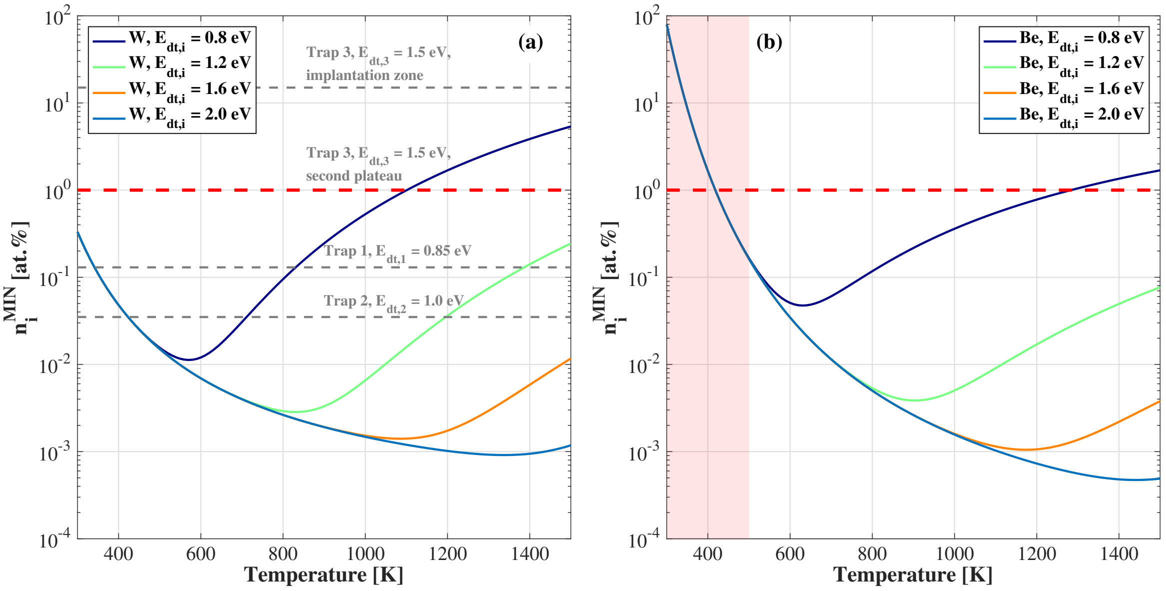

Figure 6: Minimum trap density n_i^{MIN} that must be exceeded by the traps to have a D subsurface inventory mostly found in traps (condition 16) rather than in interstitial sites. n_i^{MIN} is calculated considering extreme implantation conditions ($\Gamma_{\mathrm{imp}} = 1 \times 10^{24}$ m^{-2}.s^{-1}, $E_{\mathrm{imp}} = 1$ keV) so that the plots represent a upper limit of the condition 16. The calculation is made for both tungsten (a) and beryllium (b) considering different values of the detrapping energy. For beryllium, the red shaded region indicates the temperature range where the analytical model may be invalid as the recombination process could be rate-limiting. A dashed line is plotted in red at a trap density of 1 at.% as a guide for the eye. For tungsten, the density of traps used in the MHIMS simulations presented in this article (cf. Appendix A) are plotted in grey in figure (a). They were obtained by Hodille et al. [18] through fitting with MHIMS of the experiment of deuterium implantation in tungsten followed by thermal desorption spectrometry made by Ogorodnikova et al. [4].

n_i^{MIN} is plotted in figure 16.a and 16.b for W and Be with the parameters given in Appendices A and D, respectively. The interval of temperature is chosen representative of temperatures found in fusion devices. We consider only a single implanted specie (D) with extreme implantation conditions ($\Gamma_{\mathrm{imp}} = 1 \times 10^{24}$ m^{-2}.s^{-1}, $E_{\mathrm{imp}} = 1$ keV) to maximise $n_{\mathrm{m}}^{\mathrm{BULK}}$ and therefore n_i^{MIN}. Detrapping energies (0.8, 1.2, 1.6 and 2.0 eV) are chosen in order to span the range of energies usually found for HI traps in those materials from Density Functional Theory calculations [24, 25, 26, 27] or from fitting of thermal desorption spectrometry [7, 28, 10]. All curves from figure 6.a and 6.b present the same trend with both a low and a high temperature regimes. In the low-temperature regime, n_i^{MIN} is similar for all the detrapping energies: n_i^{MIN} is dominated by $n_{\mathrm{m}}^{\mathrm{BULK}}$, first term in equation 17, which is similar for all the detrapping energies. Consequently it depends on the implantation conditions and decreases with increasing temperature due to an increase of the diffusion coefficient. As n_i^{MIN} is calculated assuming extreme implantation conditions, this low-temperature regime can be seen as an upper limit. In the high-temperature regime, n_i^{MIN} increases with the temperature. The lower the detrapping energy, the lower the transition temperature between both regimes: the second term in n_i^{MIN} becomes preponderant.

While the n_i^{MIN} curves present a similar shape for both materials, they differ in terms of amplitude for similar detrapping energies. According to equation 17, this is due to the different diffusion coefficients of D in both materials[1]. Below 1000 K, the diffusion coefficient of D is higher in W than in Be, and consequently n_i^{MIN} is lower in W than in Be. Above 1000 K, D diffusion is higher in Be than in W and the minimum density of traps is lower.

In figure 16, a red and dashed horizontal line is plotted at $n_i^{\mathrm{MIN}} = 1$ at.%. For W, any traps with such density and a detrapping energy above 1.2 eV satisfies the condition 16 in all the temperature range. For Be, above 500 K, one can note that any trap with a detrapping energy above 1.2 eV and with a density above 1 at.% satisfies the condition 16. Below 500 K (red shaded area in figure 16.b), recombination may be rate-limiting [10] and the validity of the analytical model is not guaranteed. This would lead to an increase of the density of interstitial HI and therefore an increase of n_i^{MIN}.

One will see if the condition on the trap density, equation 16, is fulfilled by traps reported in the literature. First, for W, one will consider the traps used in the MHIMS simulations presented in the previous sections. These traps were identified by Hodille et al. [18] through fitting with MHIMS of the experiment of D implantation in W followed by thermal desorption spectrometry made by Ogorodnikova et al. [4]. Three traps were identified with respective detrapping energies $E_{\mathrm{dt},1} = 0.85$ eV, $E_{\mathrm{dt},2} = 1.00$ eV and $E_{\mathrm{dt},3} = 1.50$ eV. First, we focus on trap 3, which has the highest trap density (cf. traps profiles in figure 7). This trap has a first plateau in the implantation zone with a density $n_3 = 16$ at.% up to 30 nm and a second plateau at $n_3 = 1$ at.% from 30 nm up to 1 μm. Consequently, trap 3 fulfills the condition $n_3 \gg n_3^{\mathrm{MIN}}$ given by equation 16 in all the temperature range and hosts the majority of the D inventory under any implantation conditions. Regarding traps 1 and 2, their trap densities are uniform and are equal to $n_1 = 0.13$ at.% and $n_2 = 0.035$ at.% respectively. From figure 6.a, the condition 16 is fulfilled in a limited temperature region. In the low-temperature region, this condition is not fulfilled for both traps between 300 and 400 K. However, a factor of 10 decrease in the implantation flux density ($10^{24} \rightarrow 10^{23}$ D.m^{-2}.s^{-1}, which is still a strong flux density) would lead to a similar decrease in $n_{\mathrm{m}}^{\mathrm{BULK}}$ and therefore in n_i^{MIN} in the low-temperature region. Thus, $n_1 \gg n_1^{\mathrm{MIN}}$ and $n_2 \gg n_2^{\mathrm{MIN}}$ are satisfied in the low-temperature region. The temperature range of validity of the analytical model for W, where the full inventory is found in traps, is as follows:

- trap 1, for 300 K $\leq T \leq$ 800 K
- trap 2, for 300 K $\leq T \leq$ 1000 K
- trap 3, full range of temperature

For Be, Matveev et al. have fitted the saturated high-temperature peak ($>$ 500 K) observed in thermal desorption spectrometry of D implanted Be at room temperature made by Oberkofler considering a density of vacancies of 14 at.% extending to 50 nm depth with a detrapping energy $E_{\mathrm{dt}} = 1.5$ eV and a detrapping pre-exponential factor $\nu_{\mathrm{dt}}^0 = 10^{12}$ s^{-1} [10]. Consequently, from figure 6.b, we see that this density of vacancies is way above n_i^{MIN} and we conclude that vacancies in Be will host the majority of the inventory under any implantation conditions[2]. Also in reference [29], the high-temperature desorption peak observed in the thermal desorption spectrometry made by Reinelt et al. after D implantation in Be at room temperature was fitted with the MHIMS code assuming one trap

---

[1] In the high-temperature regime, n_i^{MIN} also differs for the two materials due to different terms $\lambda^2 n_{\mathrm{IS}}$. However, this term is slightly higher for Be than for W (by a factor of ~ 1.3).

[2] It must be noted that Matveev et al. have used a lower pre-exponential factor for detrapping ν_{dt}^0 than the one used to calculate n_i^{MIN} in figure 6.b. However, according to equation 17, a lower ν_{dt}^0 would lead to a lower n_i^{MIN} than in figure 6.b and our conclusion is still valid.

with $E_{\mathrm{dt},1} = 1.82$ eV, $\nu^0_{\mathrm{dt},1} = 10^{13}$ s^{-1} and $n_1 = 10.3$ at.% extending to 60 nm depth. Again, the condition $n_1 \gg n_1^{\mathrm{MIN}}$ is valid in the full temperature range and the majority of the inventory is found in the beryllium traps.

To summarise, the HI subsurface inventory is fully dominated by trapped HIs:

- in W: in all the temperature range, if there is a trap i with a density $n_i \geq 1$ at.% and a detrapping energy $E_{\mathrm{dt},i} \geq 1.2$ eV
- in Be: for $T \geq 500$ K, if there is a trap i with a density $n_i \geq 1$ at.% and a detrapping energy $E_{\mathrm{dt},i} \geq 1.2$ eV

We have shown that such traps are reported in the literature and we conclude that the HI subsurface inventory in W and Be is dominated by trapped HIs during plasma implantation.

7 Conclusions.

An analytical model for hydrogen inventory saturation in the subsurface (several micrometers depth) under plasma implantation has been derived. This model was compared to non-linear Reaction-Diffusion simulations of deuterium implantation in tungsten at three different material temperatures. A good agreement is observed between the profiles of mobile/interstitial deuterium and trapped deuterium at the subsurface given by the analytical model and by the Reaction-Diffusion simulations for the three considered temperatures.
It was demonstrated using the analytical model that the hydrogen isotopes subsurface inventory is dominated by trapped hydrogen for both tungsten and beryllium in all the range of material temperature found in fusion devices. For beryllium, the situation is unclear below 500 K as recombination at the surface may be rate-limiting and the interstitial hydrogen may dominate the subsurface inventory. Using the analytical model, the maximum subsurface density profiles of trapped hydrogen in the trap i, $n^{\mathrm{BULK}}_{\mathrm{t},i}(x)$, is expressed as function of the trap density profile, $n_i(x)$, and of the bulk filling ratio of the trap at steady-state, $f^{\mathrm{BULK}}_{\mathrm{stat},i}$, as follows: $n^{\mathrm{BULK}}_{\mathrm{t},i}(x) = f^{\mathrm{BULK}}_{\mathrm{stat},i} n_i(x)$. $f^{\mathrm{BULK}}_{\mathrm{stat},i}$, equation 15, expresses the balance between trapping and detrapping and is function of the material temperature and of the implantation conditions (flux density and impact energy). As the subsurface hydrogen inventory is dominated by traps, $f^{\mathrm{BULK}}_{\mathrm{stat},i}$ represents a simple parameter that indicates how the total subsurface inventory builds up during plasma operation. This parameters will be used in future contributions to understand the retention dynamics observed during non-linear Reaction-Diffusion simulations.

Acknowledgements

This work has been carried out within the framework of the EUROfusion Consortium, funded by the European Union via the Euratom Research and Training Programme (Grant Agreement No 101052200 — EUROfusion). Views and opinions expressed are however those of the author(s) only and do not necessarily reflect those of the European Union or the European Commission. Neither the European Union nor the European Commission can be held responsible for them.

Appendix A: Reaction-Diffusion parameters for the simulations of deuterium implantation in tungsten.

The free-parameters of the Reaction-Diffusion equations considered for the simulations of deuterium implantation in tungsten reported in this contribution are summed up in table 3.

DIFFUSION		
Parameter	Value	From
D_0	$1.9 \times 10^{-7}/\sqrt{A}$ m^2.s^{-1}	Density Functional Theory [24]
E_{diff}	0.2 eV	Density Functional Theory [24]
$A = m_{\mathrm{D}}/m_{\mathrm{H}}$	2	—
TRAPPING		
Parameter	Value	From
$\nu^0_{\mathrm{t},i}$	$D_0/{\lambda_{\mathrm{W}}}^2$	—
λ_{W}	111.7 pm	Experiment [30] and Density Functional Theory [24]
$E_{\mathrm{t},i}$	0.2 eV	—
n_{IS}	$6\rho_{\mathrm{W}}$	Density Functional Theory [24]
ρ_{W}	6.3382×10^{28} m^{-3}	[31]
DETRAPPING		
Parameter	Value	From
$\nu^0_{\mathrm{dt},i}$	10^{13} s^{-1}	—

Table 3: Parameters of the Reaction-Diffusion equations considered for simulations of D implantation in W.

Regarding the W traps that can accommodate D, the detrapping energies and trap density profiles defined by Hodille et al. [18] are used. They were obtained through fitting with the Reaction-Diffusion code MHIMS of the experiment of D implantation in W followed by thermal desorption spectrometry made by Ogorodnikova et al. [4]. Three traps are considered: two intrinsic traps and one trap induced by plasma irradiation. Their profiles are displayed in figure 7. The intrinsic traps 1 and 2 have a flat depth profile and were respectively attributed to dislocations and/or iron impurities and to grain boundaries. The plasma-induced trap 3 presents two damaged zones: a highly damaged zone in the implantation zone, attributed to thermodynamic formation of vacancies [32] and often referred to as *super-saturated layer*, and a damaged zone extending in the depth of the material, attributed to vacancies filled with light impurities (e.g. oxygen or carbon). These parameters are considered to be appropriate for a W material submitted to divertor-like irradiation conditions.

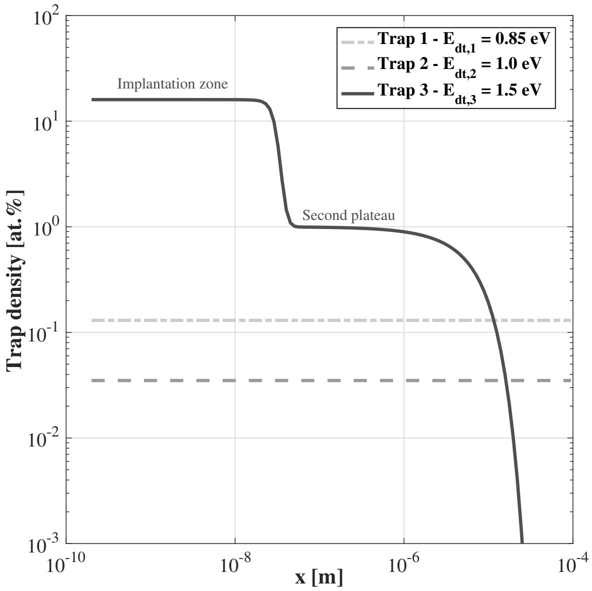

Figure 7: Density profiles of traps and related detrapping energies used in the simulation of D implantation in W. The densities are expressed in atomic fraction of W (%).

Appendix B: Interval of validity of the analytical model for the case of Dirichlet boundary condition at the rear surface.

The exact solution of the diffusion equation 8 considering a Dirichlet B.C. at $x = L$, $n_{\mathrm{m}}^{\mathrm{D}}$, can be expressed as a function of the exact solution of the same equation for the case of Neumann B.C., $n_{\mathrm{m}}^{\mathrm{N}}$ (given by equation 9), and of $n_{\mathrm{m}}^{\mathrm{BULK}}$ (equation 9c):

$$\forall\, x \in [0, L],\, n_{\mathrm{m}}^{\mathrm{D}}(x) = n_{\mathrm{m}}^{\mathrm{N}}(x) - n_{\mathrm{m}}^{\mathrm{BULK}} \frac{x}{L} \tag{18}$$

Thus, the approximation of $n_{\mathrm{m}}^{\mathrm{D}}$ by $n_{\mathrm{m}}^{\mathrm{N}}$ gives an absolute error δ_{a} on $n_{\mathrm{m}}^{\mathrm{D}}$:

$$\forall\, x \in [0, L],\, \delta_{\mathrm{a}}(x) = \left| n_{\mathrm{m}}^{\mathrm{D}}(x) - n_{\mathrm{m}}^{\mathrm{N}}(x) \right| = n_{\mathrm{m}}^{\mathrm{BULK}} \frac{x}{L} \tag{19}$$

δ_{a} increases with x. For a maximum tolerated error of $k_{\%} n_{\mathrm{m}}^{\mathrm{BULK}}$, the approximation of $n_{\mathrm{m}}^{\mathrm{D}}$ by $n_{\mathrm{m}}^{\mathrm{N}}$ is valid up to $x = k_{\%} L$:

$$\forall\, x \in [0, k_{\%} L],\, n_{\mathrm{m}}^{\mathrm{D}}(x) \approx n_{\mathrm{m}}^{\mathrm{N}}(x) \tag{20}$$

We are interested in the case where the plateau $n_{\mathrm{m}}^{\mathrm{D}}(x) \approx n_{\mathrm{m}}^{\mathrm{BULK}}$ for $x > X_{\mathrm{imp},2}$ exists. This sets a minimum value of the material length L:

$$\exists\, x \in [X_{\mathrm{imp},2}, L] \mid n_{\mathrm{m}}^{\mathrm{D}}(x) \approx n_{\mathrm{m}}^{\mathrm{BULK}} \Leftrightarrow \delta_{\mathrm{a}}(X_{\mathrm{imp},2}) \ll k_{\%} n_{\mathrm{m}}^{\mathrm{BULK}} \Leftrightarrow L \gg \frac{X_{\mathrm{imp},2}}{k_{\%}} \tag{21}$$

Appendix C: Exact solutions of the diffusion equation 1a with source terms at steady-state and error estimation of the analytical model.

At steady-state, the diffusion equation 1a of the Reaction-Diffusion system becomes linear and can be solved analytically. We herein provide the resolution of this equation. We first generalise this equation at steady-state by considering a given number of external sources N_S:

$$\begin{cases} \dfrac{\partial}{\partial x}\left(D(T)\dfrac{\partial n_\mathrm{m}}{\partial x}\right)+\displaystyle\sum_{j=1}^{N_\mathrm{S}} S^j_\mathrm{ext}(x)=0 & \text{(22a)}\\ \text{B.C. at } x=0\text{: } n_\mathrm{m}(0)=0 & \text{(22b)}\\ \text{B.C. at } x=L\text{: } \left| \begin{array}{l} \text{Dirichlet B.C.: } n_\mathrm{m}(L)=0 \\ \qquad\qquad \text{or} \\ \text{Neumann B.C.: } D(T)\dfrac{\partial n_\mathrm{m}}{\partial x}(L)=0 \end{array}\right. & \text{(22c)} \end{cases}$$

By invoking the superposition theorem, the solutions $n^{BC}_\mathrm{m}(x)$ of the diffusion equation 22 can be expressed as follows:

$$n^{BC}_\mathrm{m}(x)=\sum_{j=1}^{N_\mathrm{S}}\left\{\int_0^L G^{BC}(x,y)S^j_\mathrm{ext}(y)\,dy\right\} \tag{23}$$

where BC is the type of B.C. considered at $x=L$. $G^{BC}(x,y)$ is the impulse response / the Green function of the system 22, solution of the following auxiliary problem:

$$\begin{cases} \dfrac{\partial}{\partial x}\left(D(T)\dfrac{\partial G^{BC}(x,y)}{\partial x}\right)+\delta(x-y)=0 & \text{(24a)}\\ \text{B.C. at } x=0\text{: } G^{BC}(0,y)=0 & \text{(24b)}\\ \text{B.C. at } x=L\text{: } \left| \begin{array}{l} \text{Dirichlet B.C.: } G^{BC}(L,y)=0 \\ \qquad\qquad \text{or} \\ \text{Neumann B.C.: } D(T)\dfrac{\partial G^{BC}}{\partial x}(L,y)=0 \end{array}\right. & \text{(24c)} \end{cases}$$

where $\delta(x-y)$ is the Dirac function. The diffusion equation in the auxiliary system, equation 24a, is similar to the diffusion equation 8 used to derive the analytical model in section 4.

For the case of Neumann B.C. at $x=L$, the Green function $G^\mathrm{N}(x,y)$ can be expressed using equation 9:

$$\begin{cases} \forall\ x\in[0,y],\ G^\mathrm{N}(x,y)=\dfrac{x}{D(T)} & \text{(25a)}\\ \forall\ x\in[x,L],\ G^\mathrm{N}(x,y)=\dfrac{y}{D(T)} & \text{(25b)} \end{cases}$$

The density of mobile is then expressed as follows:

$$n^\mathrm{N}_\mathrm{m}(x)=\frac{1}{D(T)}\sum_{j=1}^{N_\mathrm{S}}\left\{\int_0^x yS^j_\mathrm{ext}(y)\,dy+x\int_x^L S^j_\mathrm{ext}(y)\,dy\right\} \tag{26}$$

For the case of Dirichlet B.C. at $x=L$, the Green function $G^\mathrm{D}(x,y)$ is expressed as a function of $G^\mathrm{N}(x,y)$ using equation 18:

$$\forall\ x\in[0,L],\ G^\mathrm{D}(x,y)=G^\mathrm{N}(x,y)-\frac{y}{D(T)}\frac{x}{L} \tag{27}$$

and the resulting density of mobile is expressed as follows:

$$n_{\mathrm{m}}^{\mathrm{D}}(x) = n_{\mathrm{m}}^{\mathrm{N}}(x) - \frac{1}{D(T)} \frac{x}{L} \sum_{j=1}^{N_{\mathrm{S}}} \left\{ \int_0^L y S_{\mathrm{ext}}^{j}(y)\, dy \right\} \tag{28}$$

To calculate the expressions of $n_{\mathrm{m}}^{\mathrm{N}}(x)$ and $n_{\mathrm{m}}^{\mathrm{D}}(x)$, one must specify a profile of the external HI sources. It is usually considered as a gaussian defined by a mean implantation range of particles X_{imp}^{j} and a standard deviation $\sigma_{\mathrm{imp}}^{j}$. Both parameters can be provided by Binary Collision Approximation codes such as SRIM [19] or SDTrim.sp [20].

$$S_{\mathrm{ext}}^{j}(x) = \frac{K^j \mathit{\Gamma}_{\mathrm{imp}}^{j}}{\sqrt{2\pi}\sigma_{\mathrm{imp}}^{j}} \exp\left(- \frac{\left(x - X_{\mathrm{imp}}^{j}\right)^2}{2{\sigma_{\mathrm{imp}}^{j}}^2} \right) \tag{29}$$

where K^j is a normalisation factor defined as follows:

$$\int_0^L S_{\mathrm{ext}}^{j}(x)\, dx = \mathit{\Gamma}_{\mathrm{imp}}^{j} \Leftrightarrow K^j = \frac{2}{\operatorname{erf}\left(\dfrac{L - X_{\mathrm{imp}}^{j}}{\sqrt{2}\sigma_{\mathrm{imp}}^{j}} \right) + \operatorname{erf}\left(\dfrac{X_{\mathrm{imp}}^{j}}{\sqrt{2}\sigma_{\mathrm{imp}}^{j}} \right)} \tag{30}$$

Then the expressions of the mobile density become:

$$\begin{aligned} n_{\mathrm{m}}^{\mathrm{N}}(x) = \frac{1}{D(T)} \sum_{j=1}^{N_{\mathrm{S}}} \frac{K^j \mathit{\Gamma}_{\mathrm{imp}}^{j}}{2} \Bigg\{ & x \operatorname{erf}\left(\frac{L - X_{\mathrm{imp}}^{j}}{\sqrt{2}\sigma_{\mathrm{imp}}^{j}} \right) \\ & + \sqrt{2}\sigma_{\mathrm{imp}}^{j} \left[- \operatorname{ierf}\left(\frac{x - X_{\mathrm{imp}}^{j}}{\sqrt{2}\sigma_{\mathrm{imp}}^{j}} \right) + \operatorname{ierf}\left(\frac{X_{\mathrm{imp}}^{j}}{\sqrt{2}\sigma_{\mathrm{imp}}^{j}} \right) \right] \Bigg\} \end{aligned} \tag{31}$$

$$\begin{aligned} n_{\mathrm{m}}^{\mathrm{D}}(x) = n_{\mathrm{m}}^{\mathrm{N}}(x) + \frac{1}{D(T)} \frac{x}{L} \sum_{j=1}^{N_{\mathrm{S}}} \frac{K^j \mathit{\Gamma}_{\mathrm{imp}}^{j}}{2} \Bigg\{ & \sqrt{2}\sigma_{\mathrm{imp}}^{j} \left[\operatorname{ierf}\left(\frac{L - X_{\mathrm{imp}}^{j}}{\sqrt{2}\sigma_{\mathrm{imp}}^{j}} \right) - \operatorname{ierf}\left(\frac{X_{\mathrm{imp}}^{j}}{\sqrt{2}\sigma_{\mathrm{imp}}^{j}} \right) \right] \\ & - L. \operatorname{erf}\left(\frac{L - X_{\mathrm{imp}}^{j}}{\sqrt{2}\sigma_{\mathrm{imp}}^{j}} \right) \Bigg\} \end{aligned} \tag{32}$$

where ierf is the integral of the error function defined as follows:

$$\operatorname{ierf}(z) = \frac{1}{\sqrt{\pi}} \exp\left(-z^2\right) + z. \operatorname{erf}(z) \tag{33}$$

We can reduce these equations by considering the following approximations:

$$x > X_{\mathrm{imp}}^{j} + 8\sigma_{\mathrm{imp}}^{j} \Rightarrow \begin{cases} \operatorname{ierf}\left(\dfrac{x - X_{\mathrm{imp}}^{j}}{\sqrt{2}\sigma_{\mathrm{imp}}^{j}} \right) \approx \dfrac{x - X_{\mathrm{imp}}^{j}}{\sqrt{2}\sigma_{\mathrm{imp}}^{j}} \\ \operatorname{erf}\left(\dfrac{x - X_{\mathrm{imp}}^{j}}{\sqrt{2}\sigma_{\mathrm{imp}}^{j}} \right) \approx 1 \end{cases} \tag{34}$$

Such approximations are especially true for $x = L$. Indeed, the maximum implantation range X_{imp}^{j} and standard deviation $\sigma_{\mathrm{imp}}^{j}$ for both W and Be are 90 nm and 25 nm respectively (for 4 eV D implantation in Be), which entails according to equation 34 that $L > 290$ nm for both approximations to be valid.

This condition is fulfilled as the material thickness is usually above 1 μm. Then the expressions 31 and 32 become:

$$n_{\mathrm{m}}^{\mathrm{N}}(x) = \frac{1}{D(T)} \sum_{j=1}^{N_{\mathrm{S}}} \frac{K^j \mathit{\Gamma}_{\mathrm{imp}}^j}{2} \left\{ x + \sqrt{2}\sigma_{\mathrm{imp}}^j \left[-\operatorname{ierf}\left(\frac{x - X_{\mathrm{imp}}^j}{\sqrt{2}\sigma_{\mathrm{imp}}^j} \right) + \operatorname{ierf}\left(\frac{X_{\mathrm{imp}}^j}{\sqrt{2}\sigma_{\mathrm{imp}}^j} \right) \right] \right\} \tag{35}$$

$$n_{\mathrm{m}}^{\mathrm{D}}(x) = n_{\mathrm{m}}^{\mathrm{N}}(x) - \frac{1}{D(T)} \frac{x}{L} \sum_{j=1}^{N_{\mathrm{S}}} \frac{K^j \mathit{\Gamma}_{\mathrm{imp}}^j}{2} \left\{ X_{\mathrm{imp}}^j + \sqrt{2}\sigma_{\mathrm{imp}}^j \operatorname{ierf}\left(\frac{X_{\mathrm{imp}}^j}{\sqrt{2}\sigma_{\mathrm{imp}}^j} \right) \right\} \tag{36}$$

Approximations 34 can be used to further simplify the expressions to obtain the exact density of mobile in the bulk direction $n_{\mathrm{m,e}}^{\mathrm{BULK}}$:

$$\forall\, x \in \left[X_{\mathrm{imp}}^j + 8\sigma_{\mathrm{imp}}^j, L \right],$$

$$n_{\mathrm{m}}^{\mathrm{N}}(x) \approx n_{\mathrm{m,e}}^{\mathrm{BULK}} = \frac{1}{D(T)} \sum_{j=1}^{N_{\mathrm{S}}} \mathit{\Gamma}_{\mathrm{imp}}^j X_{\mathrm{imp}}^j \left\{ 1 + \frac{1}{1 + \operatorname{erf}\left(\frac{X_{\mathrm{imp}}^j}{\sqrt{2}\sigma_{\mathrm{imp}}^j} \right)} \frac{\sqrt{2}\sigma_{\mathrm{imp}}^j}{\sqrt{\pi} X_{\mathrm{imp}}^j} \exp\left(-\frac{{X_{\mathrm{imp}}^j}^2}{2{\sigma_{\mathrm{imp}}^j}^2} \right) \right\} \tag{37}$$

$$n_{\mathrm{m}}^{\mathrm{D}}(x) \approx n_{\mathrm{m,e}}^{\mathrm{BULK}} - \frac{1}{D(T)} \frac{x}{L} \sum_{j=1}^{N_{\mathrm{S}}} \frac{K^j \mathit{\Gamma}_{\mathrm{imp}}^j}{2} \left\{ X_{\mathrm{imp}}^j + \sqrt{2}\sigma_{\mathrm{imp}}^j \operatorname{ierf}\left(\frac{X_{\mathrm{imp}}^j}{\sqrt{2}\sigma_{\mathrm{imp}}^j} \right) \right\} \tag{38}$$

From the equation 37, one can see that $n_{\mathrm{m}}^{\mathrm{BULK}}$ given by the analytical model, equation 9c, underestimates the value of mobile density in the bulk. The relative error on $n_{\mathrm{m}}^{\mathrm{BULK}}$ is then bounded:

$$\frac{\delta n_{\mathrm{m}}}{n_{\mathrm{m}}} = \left| \frac{n_{\mathrm{m}}^{\mathrm{BULK}} - n_{\mathrm{m,e}}^{\mathrm{BULK}}}{n_{\mathrm{m,e}}^{\mathrm{BULK}}} \right| < \max \left\{ \frac{1}{1 + \left[1 + \operatorname{erf}\left(\frac{X_{\mathrm{imp}}^j}{\sqrt{2}\sigma_{\mathrm{imp}}^j} \right) \right] \frac{\sqrt{\pi} X_{\mathrm{imp}}^j}{\sqrt{2}\sigma_{\mathrm{imp}}^j} \exp\left(\frac{{X_{\mathrm{imp}}^j}^2}{2{\sigma_{\mathrm{imp}}^j}^2} \right)},\ j = 1..N_{\mathrm{S}} \right\} \tag{39}$$

The maximum relative error can be estimated from SRIM implantation tables. It is about 5 % for W in all the impact energy and angle of incidence ranges found in fusion devices. For Be, it ranges from 6 % for normal incidence to 12 % for grazing-incidence angles. Then the corresponding relative error on the stationary bulk filling ratio of traps $f_{\mathrm{stat},i}^{\mathrm{BULK}}$, and therefore on the density of trapped HI, is:

$$\frac{\delta f_{\mathrm{stat},i}}{f_{\mathrm{stat},i}} = \frac{1}{1 + \frac{\nu_{\mathrm{t},i}^*(T)}{\nu_{\mathrm{dt},i}(T)} \frac{n_{\mathrm{m}}(x)}{n_{\mathrm{IS}}}} \frac{\delta n_{\mathrm{m}}}{n_{\mathrm{m}}} \leq \frac{\delta n_{\mathrm{m}}}{n_{\mathrm{m}}} \tag{40}$$

This error is below the one on the mobile density, and therefore below 5 % for W and below 12 % for Be.

Appendix D: Reaction-Diffusion parameters considered for deuterium implantation in beryllium.

DIFFUSION		
Parameter	Value	From
D_0	$1.89 \times 10^{-6}/\sqrt{A}$ $m^2.s^{-1}$	Kinetic Monte-Carlo [10] [33]
E_{diff}	0.4 eV	Kinetic Monte-Carlo [10] [33]
$A = m_{\text{D}}/m_{\text{H}}$	2	—
TRAPPING		
Parameter	Value	From
$\nu^0_{\text{t},i}$	$D_0/{\lambda_{\text{Be}}}^2$	—
λ_{Be}	157.7 pm	Density Functional Theory [34]
$E_{\text{t},i}$	0.4 eV	—
n_{IS}	$2\rho_{\text{Be}}$	Density Functional Theory [34]
ρ_{Be}	12.2×10^{28} m^{-3}	[35]
DETRAPPING		
Parameter	Value	From
$\nu^0_{\text{dt},i}$	10^{13} s^{-1}	—

Table 4: Parameters of the Reaction-Diffusion equations considered for deuterium implantation in beryllium.

References

[1] S. Brezinsek et al. Fuel retention studies with the ITER-Like Wall in JET. Nuclear Fusion, 53(8):083023, 2013.

[2] A. McNabb and P. K. Foster. A new analysis of the diffusion of hydrogen in iron and ferritic steels. Transactions of the Metallurgical Society of AIME, 227(3):618, 1963.

[3] C. García-Rosales et al. Re-emission and thermal desorption of deuterium from plasma sprayed tungsten coatings for application in ASDEX-upgrade. Journal of Nuclear Materials, 233-237:803 – 808, 1996.

[4] O. V. Ogorodnikova et al. Deuterium retention in tungsten in dependence of the surface conditions. Journal of Nuclear Materials, 313-316:469 – 477, 2003. Plasma-Surface Interactions in Controlled Fusion Devices 15.

[5] M. Poon et al. Modelling deuterium release during thermal desorption of D+-irradiated tungsten. Journal of Nuclear Materials, 374(3):390 – 402, 2008.

[6] K. Schmid et al. Comparison of hydrogen retention in W and W/Ta alloys. Journal of Nuclear Materials, 426(1):247 – 253, 2012.

[7] E. A. Hodille et al. Macroscopic rate equation modeling of trapping/detrapping of hydrogen isotopes in tungsten materials. Journal of Nuclear Materials, 467:424 – 431, 2015.

[8] J. Guterl et al. Theoretical analysis of deuterium retention in tungsten plasma-facing components induced by various traps via thermal desorption spectroscopy. Nuclear Fusion, 55(9):093017, aug 2015.

[9] R. Piechoczek et al. Deuterium trapping and release in Be(0001), Be(11–20) and polycrystalline beryllium. Journal of Nuclear Materials, 438:S1072 – S1075, 2013. Proceedings of the 20th International Conference on Plasma-Surface Interactions in Controlled Fusion Devices.

[10] D. Matveev et al. Reaction-diffusion modeling of hydrogen transport and surface effects in application to single-crystalline Be. Nuclear Instruments and Methods in Physics Research Section B: Beam Interactions with Materials and Atoms, 430:23 – 30, 2018.

[11] R. A. Oriani. The diffusion and trapping of hydrogen in steel. Acta Metallurgica, 18(1):147 – 157, 1970.

[12] A. H. M. Krom and Ad. Bakker. Hydrogen trapping models in steel. Metallurgical and Materials Transactions B, 31(6):1475–1482, Dec 2000.

[13] C. Quirós et al. Blister formation and hydrogen retention in aluminium and beryllium: A modeling and experimental approach. Nuclear Materials and Energy, 12:1178 – 1183, 2017. Proceedings of the 22nd International Conference on Plasma Surface Interactions 2016, 22nd PSI.

[14] J. Denis et al. Dynamic modelling of local fuel inventory and desorption in the whole tokamak vacuum vessel for auto-consistent plasma-wall interaction simulations. Nuclear Materials and Energy, 19:550 – 557, 2019.

[15] B. L. Doyle. A simple theory for maximum H inventory and release: A new transport parameter. Journal of Nuclear Materials, 111-112:628 – 635, 1982.

[16] K. Schmid and M. Zibrov. On the use of recombination rate coefficients in hydrogen transport calculations. Nuclear Fusion, 61(8):086008, jun 2021.

[17] K. Schmid. Diffusion-trapping modelling of hydrogen recycling in tungsten under ELM-like heat loads. Physica Scripta, T167:014025, jan 2016.

[18] E. A. Hodille. Study and modeling of the deuterium trapping in ITER relevant materials. Theses, UNIVERSITE D'AIX-MARSEILLE, November 2016.

[19] J. F. Ziegler, M. D. Ziegler, and J. P. Biersack. SRIM – The stopping and range of ions in matter (2010). Nuclear Instruments and Methods in Physics Research Section B: Beam Interactions with Materials and Atoms, 268(11):1818 – 1823, 2010. 19th International Conference on Ion Beam Analysis.

[20] A. Mutzke, R. Schneider, W.Eckstein, R.Dohmen, K.Schmid, U. von Toussaint, and G.Bandelow. SDTrimSP Version 6.00. IPP Report 2019-02, 2019.

[21] J. Ehrenberg, V. Philipps, L. De Kock, R.A. Causey, and W.L. Hsu. Analysis of deuterium recycling in JET under beryllium first wall conditions. Journal of Nuclear Materials, 176-177:226 – 230, 1990.

[22] T. Loarer et al. Gas balance and fuel retention in fusion devices. Nuclear Fusion, 47(9):1112–1120, aug 2007.

[23] V. Philipps et al. Dynamic fuel retention and release under ITER like wall conditions in JET. Journal of Nuclear Materials, 438:S1067 – S1071, 2013. Proceedings of the 20th International Conference on Plasma-Surface Interactions in Controlled Fusion Devices.

[24] N. Fernandez et al. Hydrogen diffusion and vacancies formation in tungsten: Density Functional Theory calculations and statistical models. Acta Materialia, 94:307 – 318, 2015.

[25] A De Backer, D R Mason, C Domain, D Nguyen-Manh, M-C Marinica, L Ventelon, C S Becquart, and S L Dudarev. Hydrogen accumulation around dislocation loops and edge dislocations: from atomistic to mesoscopic scales in BCC tungsten. Physica Scripta, T170:014073, nov 2017.

[26] Laura Ferry. Contribution à l'étude du comportement du tritium dans le béryllium (contexte ITER). Theses, Aix-Marseille Université (AMU), November 2017.

[27] L. Ferry et al. Tritium behaviour in beryllium investigated by DFT. In presented at the 16th International Conference on Plasma-Facing Materials and Components, Neuss, Germany, 16–19 May 2017.

[28] M. Zibrov, S. Ryabtsev, Yu. Gasparyan, and A. Pisarev. Experimental determination of the deuterium binding energy with vacancies in tungsten. Journal of Nuclear Materials, 477:292–297, 2016.

[29] Julien Denis. Dynamic modelling of local fuel desorption and retention in the wall of nuclear fusion reactors for auto-consistent plasma-wall interaction simulations. Theses, Aix-Marseille Université (AMU), December 2019.

[30] V. T. Deshpande and R. Pawar. X-Ray determination of the thermal expansion of tungsten. Current Science, 31(12):497–499, 1962.

[31] H. Pastor. Propriétés du tungstène et de ses alliages. Techniques de l'ingénieur Métaux et alliages non ferreux, base documentaire : TIB357DUO.(ref. article : m570), 1985. fre.

[32] E. A. Hodille, N. Fernandez, Z. A. Piazza, M. Ajmalghan, and Y. Ferro. Hydrogen supersaturated layers in H/D plasma-loaded tungsten: A global model based on thermodynamics, kinetics and density functional theory data. Phys. Rev. Materials, 2:093802, Sep 2018.

[33] M. Wensing. Reaction-diffusion modelling of hydrogen retention and release mechanisms in beryllium. Master thesis, Aachen University, 2016.

[34] L. Ferry et al. Theoretical investigation on the point defect formation energies in beryllium and comparison with experiments. Nuclear Materials and Energy, 12:453 – 457, 2017. Proceedings of the 22nd International Conference on Plasma Surface Interactions 2016, 22nd PSI.

[35] V. Barabash. Summary of material properties for structural analysis of the ITER internal components. ITER Organization.